



HAL
open science

Simultaneous imaging of soot volume fraction, PAH, and OH in a turbulent n-heptane spray flame

Irfan Mulla, Bruno Renou

► To cite this version:

Irfan Mulla, Bruno Renou. Simultaneous imaging of soot volume fraction, PAH, and OH in a turbulent n-heptane spray flame. *Combustion and Flame*, 2019, 209, pp.452-466. 10.1016/j.combustflame.2019.08.012 . hal-02327911

HAL Id: hal-02327911

<https://hal.science/hal-02327911>

Submitted on 20 Dec 2021

HAL is a multi-disciplinary open access archive for the deposit and dissemination of scientific research documents, whether they are published or not. The documents may come from teaching and research institutions in France or abroad, or from public or private research centers.

L'archive ouverte pluridisciplinaire **HAL**, est destinée au dépôt et à la diffusion de documents scientifiques de niveau recherche, publiés ou non, émanant des établissements d'enseignement et de recherche français ou étrangers, des laboratoires publics ou privés.



Distributed under a Creative Commons Attribution - NonCommercial 4.0 International License

Simultaneous imaging of soot volume fraction, PAH, and OH in a turbulent *n*-heptane spray flame

Irfan. A. Mulla^{a,b,*}, Bruno Renou^{a,*}

^a*Normandie Univ., UNIROUEN, INSA Rouen, CNRS, CORIA, 76000 Rouen, France*

^b*Department of Mechanical Engineering, Imperial College London, London SW7 2AZ, UK*

Abstract

Soot formation and oxidation in a turbulent *n*-heptane jet spray flame are investigated through simultaneous imaging of quantitative soot volume fraction (f_v), flame-front (OH), and soot-precursor marked by smaller (2 to 4 ring) polycyclic aromatic hydrocarbons (PAH). Laser-induced incandescence (LII) and laser-induced fluorescence (LIF) techniques are used. The spray flame is composed of a dual branch axisymmetric structure. The inner composite branch (B1) consists of fuel-lean and non-premixed reaction zones, whereas combustion in the outer branch (B2) occurs in a non-premixed mode. Frequent local flame extinctions occur along B1, while no extinctions are observed in B2. Consequently, the soot inception occurs near B2. In the onset of soot detection ($f_v \geq 0.03$ ppm) region, soot layers are thinner than those from downstream regions where soot occupies nearly the same area as of PAH. Soot generally oxidizes across the flame-front as evidenced from the absence of soot-OH overlap. The soot structures are intermittent with peak soot probability of 60%. The most probable peak f_v measures 1 ppm, while the conditional mean is 0.42 ppm which is 2.5 times that of time-averaged f_v . Conditional mean f_v shows monotonically increasing trend with height. The flame lift-off height and local extinctions do not instantaneously influence the soot concentration, possibly due to larger convective and soot formation timescales. Soot-PAH correlations are explored.

*Corresponding authors:

Email addresses: i.mulla@imperial.ac.uk (Irfan. A. Mulla), bruno.renou@coria.fr (Bruno Renou)

Preprint submitted to Combustion and Flame

August 6, 2019

However, no strong instantaneous correlations are noted, most likely due to different chemical timescales of soot and the imaged smaller-PAH. Nevertheless, a few distinct trends are noted in soot-PAH correlations. f_v weakly increases with the PAH-LIF intensity. The PAH intensity from soot onset to peak region decreases, while both soot and PAH are nearly consumed at a local flame-tip (oxidation) region. The soot-PAH overlap decreases consistently from soot onset to oxidation region. The reported database and deduced insights can aid in the development and validation of soot models in two-phase reacting flows.

Keywords: Spray combustion, *n*-heptane, Soot, OH, PAH, Laser-induced incandescence, Laser-induced fluorescence

1. Introduction

Soot particles generated from the combustion process adversely affect our environment and health. Thus, reduction in soot emission can significantly improve the climate and human health [1]. However, soot formation is a very
5 complex process due to its high sensitivity to temperature, fuel concentration gradient, and residence time (τ). Some of these parameters fluctuate simultaneously in turbulent flows, which poses a difficulty in isolating the effect of an individual parameter. Thus, numerous investigations have been performed in laminar flames. However, combustion in practical devices is generally accom-
10 panied by turbulence. In turbulent flames, soot investigations were primarily carried out in a jet flame configuration with gaseous fuels. Past works reported a wide range of parameters namely soot particle size, soot volume fraction (f_v), temperature (T), velocity field, mixing field, qualitative polycyclic aromatic hydrocarbons (PAH), and flame-front (OH) location. The database-oriented
15 measurements include Sandia [2], Adelaide [3], and DLR [4, 5] works which contributed towards validations of simulations (e.g., [6]).

Despite the complexity of the soot formation process in turbulent flames, a few general observations can be derived from past works on gas-fueled flames. Temperature appears to be one of the crucial parameters. There are investiga-

20 tions [3, 7, 8] that suggest the occurrence of peak f_v at a preferred temperature range, typically 1200 – 1600 K. The soot formation is highly sensitive to local scalar dissipation rate (χ) [9] which is a function of the fuel concentration gradient. Soot preferentially exists in a region of low scalar dissipation rate [7]. Apart from a mixing field, velocity also influences the soot formation. Soot particles
25 exist at a preferred velocity (residence time) and local strain rate (temperature), independent of the jet exit velocity [10]. A global relationship (power-fit) was reported between the soot sheet thickness and f_v for different jet flames [11]. In general, negligible soot is noted across OH-front [12], which implies shorter soot oxidation timescales relative to flow timescales [13]. Although, soot may occa-
30 sionally survive the OH layer as suggested in [8]. Such a detailed understanding of two-phase spray flame has yet to be established.

Besides the jet configuration, soot formation was also investigated in swirl-stabilized gaseous flames [14–18]. The distinction between locally formed soot and transported soot was made in [14, 16]. The transient evolution of soot was
35 investigated through the time-resolved velocity and flame-front imaging [17]. The DLR works [14–17] provide a comprehensive database in swirl-stabilized flames, which have contributed towards the validation of large-eddy simulations (LES) [19, 20]. For a given fuel, the soot formation is governed by the air/fuel mixing and strain rate. To isolate the mixing dependence, a premixed rich flame
40 was investigated in swirl configuration [18].

To synergize the soot investigation efforts in turbulent flames, International Sooting Flame (ISF) workshop [21] has consolidated data from various groups (Sandia, DLR, Adelaide, Delft), facilitating the database access to a wider community. The available data primarily focuses on gaseous flames; however, in
45 many practical engines (especially transport) fuel is generally injected in the liquid phase. In two-phase reacting flows, further complexities arise due to the fuel droplet evaporation process. Though many soot imaging works exist in spray flames, planar quantitative studies on soot formation are scarce. Quantitative f_v has been reported in diesel engine [22] and in high-pressure vessel
50 [23].

Similar to ISF, two spray-related international workshops, namely Engine Combustion Network (ECN) [24] and Turbulent Combustion of Sprays (TCS) [25], have been established. ECN targets spray combustion in reciprocating engines, while TCS focuses on continuous spray combustion such as of gas-turbines. The ECN collaborative work [23] reported experimental and simulated f_v at a *sprayA* condition of ECN. Such quantitative soot studies in continuous spray flames are yet to be reported. Meyer et al. [26] investigated the soot formation process in swirl-stabilized spray flames using planar laser-induced fluorescence (PLIF) of OH radical and laser-induced incandescence (LII). Although qualitative, this study provided insights into the effect of equivalence ratio on soot formation. Recently, Wang et al. [27] demonstrated that the soot distribution in liquid-fueled swirl-stabilized flames is drastically different from their gas-fueled counterparts. The effect of turbulence on soot concentration and particle size was investigated through point measurements. With increasing turbulence, a sharp diminution in soot concentration was noted, while the soot particle size reduction was moderate [27].

TCS has recognized the contribution of three well-characterized experimental configurations that are appropriate for model validations. The database of the present CORIA Rouen spray burner (CRSB) [25, 28–32] is one of the target configuration along with the Sydney [33] and Cambridge [34, 35] burners. CRSB facility provides an atmospheric pressure *n*-heptane jet spray flame with co-flowing air. This turbulent flame is moderately sooting, which is ideal for pursuing the soot-focused database.

The present work links TCS and ISF efforts by providing quantitative soot volume fraction, a qualitative concentration of soot-precursor (PAH), and flame-front (OH) data in CRSB flame. Laser diagnostic techniques, namely LII, PAH-PLIF, and OH-PLIF, are applied simultaneously. Such measurements in two-phase flow enable the identification of soot onset (defined by $f_v \geq 0.03$ ppm) and oxidation zones relative to the flame-front and soot-precursor in a complex jet spray flame (containing droplets, different reaction zones, and various combustion modes [30]). The objectives of the present work are to 1) Strengthen

the CRSB database to facilitate soot model validations, 2) Identify soot onset zones relative to OH (flame-structure, local extinctions) and PAH distributions, 3) Explore spatial and intensity correlations between soot and soot-precursor (PAH).

2. Experimental methods

2.1. Burner and Flame condition

The measurements were performed in a lifted turbulent spray flame, stabilized at atmospheric pressure. The burner geometry has been detailed in a previous work [29]. Liquid-phase *n*-heptane was atomized by a simplex injector (Danfoss, 1.35 kg/h, 80° hollow cone). A non-swirling coflow of air was issued around the fuel injector through the annular opening with inner and outer diameters of 10 and 20 mm, respectively. The air and fuel flow rates were regulated using thermal and Coriolis mass flow controllers, respectively. The mass flow rate of air was 6 g/s, whereas *n*-heptane was injected at 0.28 g/s rate, leading to a global equivalence ratio of 0.71. This specific flame condition has been selected earlier [28, 29, 31] as a target case considering the flame stability and overall size.

The flame photograph is shown in Fig. 1, along with the mean progress variable of the flame-front. The mean progress variable map of the flame-front is deduced using OH-PLIF (detailed in Sec. 3.1). The Mie scattering from fuel droplets is marked by a traversing laser beam (green) in the photograph. Numerous fine droplets are present in the spray core region. The flame stabilizes at a mean height of ~ 25 mm above the burner, with a standard deviation of 0.9 mm. A double flame structure typically associated with the jet spray flame is observed. The blue flame-base suggests partial premixing, while downstream region shows yellow luminosity from soot radiation, suggesting either non-premixed or fuel-rich mode of combustion. Thus, the soot-precursor (PAH) presence is expected upstream of the sooting region. Two view fields (VFs), namely H1 ($r = 0 - 40$ mm, $z = 19 - 89$ mm) and H2 ($r = 0 - 40$ mm,

$z = 39 - 109 \text{ mm}$) were used for laser diagnostic measurements. H1 field covers the flame-base, soot inception, and peak soot regions, whereas H2 targets the soot inception, peak, and oxidation regions. Only half of the radial domain was considered for the analysis, due to the axisymmetry.

115 2.2. Laser diagnostics

Simultaneous LII/OH/PAH imaging set-up was established, which consisted of two laser systems (283 nm and 1064 nm) and three intensified CCD cameras. Total of 2000 simultaneous LII and OH/PAH-PLIF image sets were acquired at 3.3 Hz rate during each campaign. The lasers and cameras were synchronized
120 using two pulse generators. Laser-sheets propagating in opposite directions were spatially superimposed within 0.3 mm. The OH-LIF and LII signal collection cameras were located perpendicular (normal) to the light-sheet on either side of the burner. The PAH camera was mounted at a minutely off-normal angle with a Scheimpflug adapter. Fields of view of all three cameras were pixel-
125 to-pixel mapped within a pixel accuracy ($\sim 70 \mu\text{m}$) by applying a polynomial transformation to calibration grid images. The transformed images measured 70 mm wide with corresponding magnification of 14.6 pixels/mm. The used field-of-view (FOV) was 70 mm tall and 40 mm wide. The details of the specific diagnostic set-up are provided next.

130 2.2.1. Laser-induced incandescence (LII)

Soot particles were heated with 1064 nm wavelength using the Nd:YAG laser (Q-smart, Quantel), and the resulting incandescence was collected at 400 nm. The use of infrared wavelength eliminates PAH interference in the LII signal [36, 37], while collection in the blue spectrum mitigates the background
135 noise from soot radiation. The LII signal was imaged on an emICCD camera (PI-MAX4: 1024 EMB, Princeton Instruments) equipped with an imaging lens (100mm f/2.8, Cerco) and 400 nm filter with FWHM of 25 nm (#86664, Edmund Optics). The camera was gated to a prompt width of 50 ns, which reduces the bias towards larger soot particles that cool down at a slower rate. The laser

140 beam was converted to a wide light-sheet (~ 0.25 mm thick) using cylindrical
($f = -33$ mm) and spherical ($f = 1000$ mm) lenses. Only a central portion of
the light-sheet was used. The LII response along the width (40 mm) of the FOV
is verified to be uniform in a laminar ethylene/air calibration flame (detailed
next).

145 To reduce the effect of shot-to-shot fluctuations of laser energy and beam
profile, LII was performed in a plateau regime of the laser fluence (energy per
unit area). A fluence curve was obtained by varying the laser energy with a
variable attenuator (containing polarizer and half-wave plate) which facilitated
energy variation at a constant pulse width. The deduced fluence curve is pro-
150 vided in Fig. S1a of the Supplementary material. The average fluence used for
the spray flame campaign was estimated to be 0.35 J/cm². The LII response
to the light-sheet profile was measured by traversing a sooting McKenna flame
($\phi = 2.3$ ethylene/air) across the light-sheet height. The time-averaged LII re-
sponse was uniform within $\pm 7\%$ (Fig. S1b). This response profile was used to
155 correct the spray flame LII data for light-sheet non-uniformity. The LII signal
was calibrated using the laser-extinction method in an ISF-listed laminar flame
configuration [21] for which the data is well-documented. The details of the
calibration set-up and data reduction procedure are provided in Sec. S2 of the
Supplement. The deduced f_v is in excellent agreement with the reported data
160 [38]. The overall uncertainty in the mean f_v is estimated to be $\pm 19\%$. The
details of various uncertainty sources and corresponding estimates are provided
in Sec. S3.

2.2.2. OH/PAH-PLIF

OH and PAH species were simultaneously excited using identical laser pulse.
165 OH radical was excited through $Q_1(6)$ line of $A-X(1,0)$ transition near 283 nm,
and the fluorescence was collected at 310 nm. The $Q_1(6)$ transition exhibits a
low temperature sensitivity [39]. The excitation wavelength was verified by com-
paring the measured excitation/emission spectrum with that of the LIFBASE
[40]. A 283 nm pulse was generated by a frequency-doubled dye laser (TDL90,

170 Quantel) which circulated Rhodamine 590 dye. The dye laser was pumped by
an Nd:YAG laser (Brilliant-B, Quantel) operating at 532 *nm*. The 283 *nm* laser
beam was converted to a ~ 0.15 *mm* thin light-sheet using a set of spherical and
cylindrical lenses. A central portion of the light-sheet (uniform within 60%)
was used. The average laser fluence is estimated to be 0.015 *J/cm*². Such a
175 low fluence is needed to avoid LII interference [41]. The light-sheet profile was
deduced by assuming a constant OH-LIF signal along a segment of partially
premixed methane/air laminar jet flame. The assumption of constant OH-LIF
intensity was verified by translating the jet flame across the light-sheet height.
The jet flame conditions were as follows: 3 *mm* tube diameter, 8 *m/s* bulk re-
180 actant velocity, and $\phi = 13$. The deduced light-sheet profile was used to correct
the OH/PAH-LIF data of the spray flame for light-sheet non-uniformity.

The OH-LIF signal was imaged on an intensified CCD camera (PI-MAX4:
1024f, Princeton Instruments) which was equipped with a UV lens (110mm f/2.8,
Cercor). The filter set containing a narrowband 315 *nm* filter with FWHM 15 *nm*
185 (#FF01-315/15-50-D, Semrock), UG11 and WG305 Schott glass, was used. The
narrowband detection eliminated the Mie scattering noise from fuel droplets and
broadband interference from PAH fluorescence. The camera was gated to 50 *ns*
relative to the laser pulse.

As PAH absorption spectra are generally broad [37], the OH-tuned laser
190 also excited PAH radicals. The PAH detection system consisted of the identical
emICCD camera and imaging lens as of LII. The PAH camera was mounted
at an off-normal angle ($\sim 15^\circ$). To focus the image, a Scheimpflug adapter was
used. A mild perspective distortion ($< 1^\circ$) was corrected using a calibration
target and mapping procedure, as indicated earlier. To collect the PAH-LIF
195 signal, a broadband filter of 377 *nm* transmission (95%) with FWHM of 50 *nm*
(#84077, Edmund Optics) was used, similar to [12]. This filter efficiently blocks
(Optical density 6) the OH-LIF signal on PAH camera. The camera was gated
to 50 *ns* relative to the laser pulse. The 283 *nm* excitation and 350 – 400 *nm*
collection results in the imaging of smaller (primarily, 2 to 4 ring) PAH [37, 42].

200 A quantitative interpretation of PAH-LIF is not trivial [43] due to multi-

ple reasons. First of all, isolated PAH detection in flames has not yet been possible due to overlapping excitation and emission spectra of different classes (rings) of PAH [43]. Consequently, temperature and quenching correction cannot be applied even assuming that the spectroscopic parameters (absorption and quenching cross-sections) of individual PAH are known. The secondary concerns are that the LIF signal may be affected by local gas composition (collisional quenching) and temperature (quenching cross-section, gas density, and Boltzmann fraction). The present PAH measurements were performed in a fuel-rich zone where the oxygen concentration is negligible [30]. Consequently, the oxygen originated quenching may not be significant. Yet, the PAH-LIF signal is treated to be qualitative due to temperature variation and unknown quenching.

3. Results and discussion

3.1. Instantaneous OH, PAH, and Soot

Figure 2 shows instantaneous fields of simultaneously acquired f_v , OH-LIF and PAH-LIF at H1. Similar fields at H2 are shown in Fig. 3, which captures the soot inception, peak soot, and local soot oxidation regions. Additional samples of instantaneous fields are provided in Sec. S4. The left panel in Fig. 2 shows the OH-LIF and f_v , whereas the right panel shows corresponding PAH-LIF along with the OH-LIF and soot isocontours for the spatial reference. The soot isocontours mark the 7% of peak intensity and 0.03 ppm. The choice of lower isocontour is influenced by the detection limit (further discussed in Sec. 3.3). Camera counts of OH and PAH are divided by 10 and 100, respectively, for convenience. The divided numbers are referred to as arbitrary units (*au*), and original intensities are referred to as camera counts. In general, instant-to-instant fluctuations in OH-LIF intensity are not significant. On the contrary, f_v and PAH signals vary significantly (in time), and thus a variable intensity scale (detailed in Sec. S4) is used for better visualization.

From instantaneous distribution in Figs. 2 and 3 (and Sec. S4), a number of observations can be made. As soot formation is sensitive to the mode of com-

230 bustion (premixed/non-premixed) and temperature, we recall some important
spray flame characteristics established in experimental [29] and simulation [30]
works. Unlike gaseous jet flames, the jet spray flame generally consists of a dou-
ble flame structure. This structure is a result of fuel concentration stratification
generated by evaporating fuel droplets. Following a previous terminology [30],
235 the inner flame branch is referred to as B1, while the outer branch is called as
B2 (labeled in Fig. 2a). The region enclosed by B1 and B2 is denoted as zone-
C, which is composed of fuel-rich vapor pool, produced from the evaporation of
droplets that have penetrated through B1. The B1 branch is composed of two
adjacent reaction zones, the inner layer of a lean-premixed zone (B1-P, towards
240 spray) and an outer layer of the diffusion reaction zone (B1-D, towards zone-C),
as demonstrated by Shum-Kivan et al. [30] through flame-index. Combustion
in the outer B2 branch primarily occurs in the diffusion mode. Frequent local
extinctions ($\sim 50\%$ of the realizations) are observed in the B1 branch. These lo-
cal extinctions are attributed to the flow strain rate and traversing fuel droplets,
245 as suggested in [29]. The temporal frequency of local extinctions and local in-
tegral time scales were close to each other [29]. The LES work [30] indicates
the lower temperature in B1 than B2 due to a relatively fuel-lean mixture, local
flame extinctions, and higher flow strain rate [29] near B1. No extinctions are
observed in the outer B2 branch.

250 The OH layer corresponding to B1 and B2 are well-defined and relatively
thin until $z = 70$ mm. From $z > 70$ mm, B1 and B2 are appear to merge.
The merging is attributed to the flame flapping which can be noted through
high-speed OH and velocity imaging reported in [29]. In addition to merging,
the OH layer spreads over a wider region, posing a difficulty in the flame-front
255 detection. Similar to previous work [31], the centerline of OH-layer is assumed
to be the flame-front. An algorithm was developed to detect the separate B1 and
B2 flame-fronts despite the merging. In case of local extinctions, the flame-front
was connected to the nearest neighbor. Some samples of the detected flame-front
(marked in magenta) along with OH-PLIF are provided in the Supplementary
260 material for reference. Flame-fronts were used to deduce the mean progress

variable map shown in Fig. 1. A region of fresh gas was marked by $c = 0$, while burnt gas region bounded by B1-B2 was assigned $c = 1$. The mean progress variable (\bar{c}) was obtained by ensemble-averaging 2000 instantaneous c maps. Further details of the flame-front and \bar{c} deductions can be found in our earlier
265 work [31].

The PAH-LIF signal is observed throughout the zone-C. Recall that the present excitation and detection set-up primarily images LIF from the smaller (2 to 4 ring) PAH. The zone-C contains combustion products at a high temperature [30]. Consequently, fuel vapor forms through the evaporation of droplets that
270 have traversed across B1, producing a fuel-rich condition. PAH exist in close vicinity of the B1 branch despite the local extinctions. The temperature range of PAH formation (700 – 1300 K [44]) is lower than that of the soot formation (1200 – 1600 K) [3, 7, 8]. Consequently, PAH can exist in low-temperature regions around local extinctions. PAH peak occurs at an approximately equal
275 radial distance from B1 and B2. PAH near B2 branch is absent in a region below $z \approx 50$ mm (e.g., Fig. 3d). In this region, the temperature in B2 (interpreted from OH-LIF in Sec. 3.2) appears to be high. A high temperature can spatially accelerate the conversion of smaller-PAH to larger-PAH [43] that do not produce fluorescence with UV excitation [37]. Larger-PAH coagulate and go through
280 further thermochemical processes to eventually form a nascent soot particle [45]. There is a significant instant-to-instant variation in PAH-LIF intensity. In the present turbulent two-phase flow, the droplet evaporation may lead to non-uniformity in the scalar dissipation rate, which could affect the naphthalene formation as suggested in [9].

285 Next, the soot structures are discussed in the context of OH and PAH spatial patterns. In the present flame, soot exists primarily in zone-C. f_v fluctuates widely from instant-to-instant as well as spatially. Recall, the soot formation peaks at a preferred temperature of around 1400 K [3, 7, 8]. In the soot onset region, LES data [30, 46] indicates RMS fluctuations of 115 K at locations where
290 the mean temperature is 1400 K. Thus, the temperature variations may contribute to f_v fluctuations. Besides the temperature, residence time and scalar

dissipation rate fluctuations influence f_v . No soot or PAH is observed (or transported) in the spray jet core ($r = 0$), partly due to the absence of an inner recirculation zone. Note that, even in a swirl-stabilized liquid-fueled spray flame, no
295 soot was observed in the inner recirculation zone [27], unlike that of gas-fueled swirl-stabilized flames [15].

Three localized regions representing the soot onset, growth, and oxidation are discussed below. The present LII set-up was unable to detect the low soot concentrations associated with the inception. Therefore, the onset of soot de-
300 tection (OSD) by LII is defined based on a threshold of $f_v = 0.03 \text{ ppm}$.

1. *Onset*: The onset of soot detection is always observed in the vicinity of the outer branch B2, possibly due to longer residence time. In the inception region (typically, $z < 70 \text{ mm}$ zone), soot is more localized than PAH due to low diffusivity of soot particles [9]. Radially, the peak- f_v occurs at a larger
305 distance than that of the peak-PAH. The radial order of the species is as follows: the inner branch B1, PAH, soot, and the outer branch B2. The potential reasons for such flame-soot structure are provided next by using the understanding from gas-phase flames and LES data [30] of the present spray flame. In gas-phase jet flames, generally, the radial order is as fol-
310 lows: fuel-stream, PAH, soot, and the diffusion reaction zone. However, in jet spray flame, the central region upstream of B1 contains primarily finer fuel droplets which lead to a fuel-lean gas-phase mixture. Consequently, combustion in the inner layer of B1 (B1-P) occurs in a lean-premixed mode (recall Sec. 3.1). Thus, no soot is formed upstream of B1. The outer layer
315 of B1 (B1-D) contains a non-premixed reaction zone that is supported by excess oxidizer available from products of B1-P and fuel vapor from zone-C. Although the scalar dissipation rate may be favorable between B1-D and zone-C, the temperature is lower in B1 [30] due to frequent local extinctions. Additionally, the residence time is relatively shorter. Therefore, soot incep-
320 tion is not observed near B1, as conditions (χ, T, τ) are not optimum. Past B1, the interior zone-C contains fuel-rich mixture due to evaporation of larger

droplets owing to hot combustion products from B1. The LES data indicates a higher temperature in the outer diffusion reaction zone B2. Additionally, the residence time near B2 is longer. Therefore, various conditions, namely
 325 scalar dissipation rate, gas temperature, and residence time, are favorable in the inner vicinity of B2. This leads to the inception of soot near B2. The processes in the region from zone-C to B2 are analogous to the non-premixed gas-phase jet flames. Axially, PAH exists in the immediate vicinity of the flame-base, while the onset of soot-LII occurs well-downstream of the PAH
 330 inception, suggesting a relatively large time-scale of soot formation. Overall, the soot sheets are continuous without any segmentation. The lower turbulence level of the present flame (relative to swirl-stabilized flames [14, 17]) facilitates spatially continuous soot-favorable condition.

2. *Growth*: At a certain downstream distance (typically, $z > 70$ mm), radial
 335 peaks of PAH and soot occasionally overlap (Figs. 2b and 3b). The f_v and PAH spatial patterns in this region are highly correlated. Soot layer occupies the entire PAH region, unlike that in the inception region. Soot is also observed near B1 branch (Fig. 3a), although the concentration is lower than that at B2. The soot presence near B1 could be either due to a local
 340 formation or the soot transport from B2 facilitated by flapping of the flame branches. Near B1, soot is present away from local extinction regions. At locally quenched regions, the temperature may be lower than needed for soot formation (~ 1400 K). Besides, the residence time near B1 is shorter than B2 as interpreted from flow fields reported in [29, 30], which consequently
 345 inhibits the soot formation.

3. *Oxidation*: Soot concentration near OH edges is negligible. In some instances (e.g., Fig. 2c) soot and PAH are engulfed by the OH roll-up, but both (soot and PAH) are retained within the OH-layer. In general, there is no overlap between soot and OH layers, since OH is a dominant soot oxidizer [47, 48].
 350 f_v decreases sharply at the B1-B2 merged local flame-tip. Note that the f_v remains appreciable just upstream of the flame-tip. These observations suggest rapid oxidation of soot across the flame-front, as argued by [13].

Soot and PAH are also present downstream of the B1-B2 merged flame-tip (see Figs. 2b, 3d, or S3d). The existence of PAH and soot in the post flame-tip regions has resulted from the flame flapping. The PAH and soot in the downstream region may exist well-before the merging of flame branches. The flame flapping may also aid in the transport of PAH/soot from upstream regions which in turn assists the soot growth in post flame-tip regions. These are the possible reasons for a large concentration of soot and PAH past the local flame-tip. Time-resolved imaging similar to [17] is needed to investigate further.

The effect of local flame extinctions on global soot concentration (peak f_v) is also analyzed. Instants with and without local extinctions (of the B1 branch) are separated. Local extinction events are identified by processing the OH-PLIF images. In this manner, statistics can be conditioned on the presence of local extinction. The ensemble-averaged peak f_v deduced from a set of instants which exhibit local extinction and from that of without extinction measured nearly the same. Additionally, the ensemble-averaged soot inception height remains identical with no influence of local extinctions. Thus, no instantaneous correlation between local extinction and global soot formation is noted. Recall, the soot inception occurs near B2 branch which does not exhibit any local extinctions. The effect of global conditions (such as local extinctions of B1) may be prevalent only after a certain time-delay, as demonstrated by Stöhr et al. [17] in swirl-stabilized flame. The authors reported a systematic time delay of 3.5 ms between the residence time fluctuation and soot intensity response. This time delay was associated with convective and soot formation chemical timescales [17]. Soot formation time delay in the present work is estimated to be $\sim 4 ms$, based on the soot inception height and flow velocity (discussed in Sec. 3.4).

3.2. Mean OH, PAH, and Soot

The time-averaged fields of OH/PAH-LIF and f_v are shown in Fig. 4. The mean data of H1 and H2 fields are combined to provide a composite image, where

data in the overlapping region are averaged. For spatial reference, contours
 of mean progress variable ($\bar{c} = 0.1, 0.5, \text{ and } 0.9$) are overlaid. The progress
 variable and mean OH-LIF are in excellent agreement, as observed in Fig. 4a.
 385 The agreement validates the data processing method adopted for the flame-
 front detection. A low OH-LIF signal is observed along the inner branch, near
 $z = 30 \text{ mm}$. This is attributed to local flame extinctions occurring in B1,
 as discussed in the previous section. At $z = 30 \text{ mm}$, the OH signal in the
 390 outer B2 branch measures maximum, which is likely attributed to the higher
 temperature of B2 [30]. However, with increasing z , the OH signal intensity
 in B2 decreases sharply. This OH reduction is potentially attributed to soot
 oxidation reactions. Although there are other species, OH is the dominant soot
 oxidizer [47, 48], which explains the present OH reduction despite the possible
 395 higher temperature in B2. The difference in OH signal between B1 and B2
 diminishes with increasing height. The OH signal increases significantly with
 B1-B2 merging (especially, around $z = 100 \text{ mm}$), which suggests possibly higher
 flame temperature.

The spatial pattern of mean PAH (Fig. 4b) closely conforms to progress
 variable contours. An appreciable PAH signal exists within $\bar{c} = 0.9$, whereas
 400 negligible PAH signal is observed between $\bar{c} = 0.9-0.5$. Recall, the present PAH-
 LIF system primarily images 2 to 4 ring PAH (smaller-PAH), while larger PAH
 also do exist. This partially explains the negligible PAH in $\bar{c} = 0.9 - 0.5$ region.
 Nevertheless, larger-PAH are expected to get consumed to eventually form soot
 405 well-before the flame-front, as noted in gas-phase flames [49]. Additionally, PAH
 survives mainly in the $700 - 1300 \text{ K}$ range [44], which is well below the flame
 temperature. Consequently, the PAH-LIF signal near the flame-front region
 ($\bar{c} = 0.5-0.1$) is largely absent. In general, PAH exist in the vicinity of both B1
 and B2 (between $\bar{c} = 0.9 - 0.5$). However, below $z = 40 \text{ mm}$, PAH signal near
 410 the B2 branch is negligible even at $\bar{c} = 0.9$. At this height, OH-LIF intensity
 measures maximum (Fig. 4a), suggesting higher temperature. As discussed
 in Sec. 3.1, high temperature can accelerate the conversion of smaller-PAH to
 larger-PAH that do not produce fluorescence when excited at a UV wavelength.

Therefore, no smaller-PAH signal is observed radially upstream of B2.

415 The mean soot structure shown in Fig. 4c is very different from PAH and
OH. Such difference has also been noted in gas-phase swirl-stabilized flames
[14]. Soot exists primarily within $\bar{c} = 0.9 - 0.5$, while negligible soot is observed
between $\bar{c} = 0.5 - 0.1$, suggesting soot oxidation near OH fronts. The peak f_v^U
(0.17 ppm) occurs at $z = 80 - 90$ mm where the smaller-PAH mean concen-
420 tration is negligible, as smaller-PAH gets converted to larger-PAH. The mean
onset of soot detection (OSD) with the present LII system is observed to occur
in the vicinity of B2, around $z = 50$ mm. At this height, soot is not observed
near B1 branch. However, with increasing height, the soot presence is noted
near both the (B1/B2) branches. As discussed earlier, local extinctions and
425 higher strain rate [29] lowers the temperature in the B1 branch, which may not
support soot formation, unlike B2. Local extinctions in B1 are nearly absent
above $z = 60$ mm, while the OH-LIF intensity is identical to B2 (Fig. 4a). Addi-
tionally, B1-B2 merged flame-tip may increase the downstream gas temperature
owing to a negative flame-stretch, analogous to a conical Bunsen flame [50]. Soot
430 can also get transported due to flame flapping, as discussed earlier. Further-
more, the local residence time increases with height (and radial distance) due to
decreasing flow velocity [30]. Consequently, an increased temperature, residence
time, and convective transport, together can lead to soot-favorable conditions
near B1 branch in downstream regions. Time-resolved measurements are, how-
435 ever, required to distinguish between the locally formed and transported soot.

3.3. Soot intermittency and conditional mean

The unconditionally averaged soot volume fraction (f_v^U) is discussed in the
previous section. Soot structures are intermittent in a turbulent field due to
high sensitivity to the mixing field, temperature, and residence time (χ , T , τ).
440 The formation of certain PAH (naphthalene) was demonstrated [9] to be highly
sensitive to scalar dissipation rate (a function of mixing field), which in turn
affects the soot concentration. Time-averaging in an intermittent soot field can
lead to biased results [13]. Therefore, in past works, along with the time-average,

an intermittency index was also evaluated [2, 51]. The intermittency index is
 445 defined as 1 when soot concentration is below a certain threshold; otherwise,
 the index is assigned 0. Conversely, the soot presence probability (P_{soot}) can be
 defined as 1 when f_v is above a certain threshold and 0 otherwise. Alternatively,
 a conditional mean f_v (f_v^C) can be deduced to isolate the intermittency effects
 [13], where samples only with the soot presence are considered in averaging.
 450 Conditional mean and time-averaged f_v are related through soot probability,
 as $f_v^C = f_v^U / P_{soot}$. Figure 5 shows the conditionally averaged fields of PAH
 and f_v along with the soot presence probability. The soot presence threshold
 is set to 0.03 *ppm* following [2]. This threshold is limited by the measurement
 noise and dynamic range of the camera. The detection limit is governed by the
 455 need to image high soot concentrations (typically, 5 *ppm*) without saturating
 the camera. Nevertheless, for validating LES against the present data, modelers
 can impose the same threshold, as realized in [6].

To ensure statistical convergence, mean is evaluated at a location where at
 least 200 conditional samples are available. Thus, the conditional mean (Fig.
 460 5b) is available only in a part of the field. The spatial pattern of soot probability
 (Fig. 5c) appears very similar to the unconditional mean (f_v^U in Fig. 4c). Soot
 probability is the highest at $z = 80$ *mm*, while f_v^U peaks at $z = 85$ *mm*. The
 peak probability is 0.6; however, in the inception and downstream regions P_{soot}
 is substantially lower.

The effect of soot intermittency is evident from the comparison of uncondi-
 465 tional (Fig. 4c) and conditional (Fig. 5b) mean f_v , which differs both in inten-
 sity and spatial distribution. The peak f_v from the conditional mean (0.42 *ppm*)
 measures nearly 2.5 times as of the time-averaged peak f_v (0.17 *ppm*). Peak f_v^U
 occurs near $z = 85$ *mm*, and subsequently drops with height. Conversely, f_v^C
 470 does not show any axial drop. The decrease in unconditional f_v is attributed
 to larger intermittency (lower probability) as observed in Fig. 5c. Similar ob-
 servations are noted in the gas-phase jet flames [13].

The identical procedure is adapted to evaluate conditional mean PAH. The
 PAH presence is determined through a threshold of 350 counts (or 3.5 *au*). The

475 choice of threshold is influenced by the measurement noise and dynamic range
of the camera, similar to f_v . Both conditional (Fig. 5a) and unconditional
(Fig. 4a) mean PAH intensities and distributions are nearly the same since
PAH is much less intermittent. Although, the peak PAH in the conditional
mean is slightly shifted downstream relative to the unconditional mean. The
480 conditional mean PAH structure is also shifted radially closer to B2 branch.

3.4. OSD height

In this section, the potential correlation between flame lift-off height and
onset of soot detection (OSD) height is analyzed. OSD height (h_{OSD}) is defined
as the lowest z location where f_v reaches 0.03 ppm . This threshold value is
485 chosen to disregard any noise safely. As discussed earlier, the detectability was
influenced by the dynamic range and corresponding camera saturation from the
desired upper f_v limit. The soot inception may occur below the present LII
detection limit. For instance, yellow flame emission (typically associated with
soot) is visible around $z = 40 \text{ mm}$ in Fig. 1, while the present LII system
490 detects the onset of soot around $z = 50 \text{ mm}$. The LII technique may not be
able to image nascent soot [52] corresponding to inception. By defining h_{OSD}
threshold, we implicitly assume that the height between actual soot inception
(say 0.1 ppb) and defined threshold (30 ppb) is constant across instant-to-instant.

The flame lift-off height (h_{lift}) is deduced using the flame-front obtained
495 from OH-PLIF (detailed in Sec. 3.1). Since the OH-LIF and f_v were acquired
simultaneously, joint statics can be evaluated to explore a possible correlation.
Figure 6 shows the joint probability density function (PDF) of OSD and lift-off
heights. PDF is evaluated from 2000 data points using a kernel density esti-
mation [53] method. The deduced quantities can be presented either as the
500 ordinary mean or the most probable (mode) value from PDF. As discussed ear-
lier, a mean can be affected by the intermittency, while the mode value is not
influenced. The most probable value of h_{lift} measures 25 mm , which is close
to the mean value. The mode h_{OSD} is 49 mm which differs slightly from the
mean (53 mm). Apparently, there is no clear correlation between h_{OSD} and

505 h_{lift} , suggesting a limited influence of global conditions. Additionally, there is
no instantaneous influence of local extinctions of B1 on h_{OSD} , as stated earlier
in Sec. 3.1. There may be a time-delay between change in global conditions
(h_{lift}) and the soot response [17]. Thus, the soot concentration does not instan-
taneously correlate with global flame conditions (h_{lift} , local extinctions, etc.).
510 The soot formation delay in the present flame is estimated subsequently.

To investigate individual distributions, PDFs of h_{lift} and h_{OSD} are plotted.
The distribution of h_{lift} in Fig. 6b appears to be Gaussian (normal). The
arithmetic mean (μ) and standard deviation (σ) are indicated on the respective
PDF. Similarly, the PDF of h_{OSD} is shown in Fig. 6c. OSD height fluctuates
515 significantly ($\sigma = 5.7 \text{ mm}$) due to high sensitivity of soot formation to local
conditions (χ, T, τ) which may vary widely in the present two-phase turbulent
flame. The effect of flame-base fluctuation can be isolated by evaluating OSD
height in flame-fixed coordinates, as shown in Fig. 6d. In this figure, the
distribution of OSD height is well described by the log-normal trend.

520 Figure 6d can be used to interpret the soot formation time delay. The
flow velocity from the flame-base ($r = 15 \text{ mm}, z = 25 \text{ mm}$) to OSD region
($r = 24 \text{ mm}, z = 51 \text{ mm}$) is approximated as 4 m/s , based on [30]. The most
probable OSD height in flame-fixed coordinates is 26 mm (see Fig. 6d), which
translates to characteristic time-scale of 6.5 ms . The chemical time-scale of soot
525 formation for *n*-heptane (vapor-phase at $\phi = 5, T = 60 \text{ }^\circ\text{C}$) fuel is expected to
be around 1 ms , based on a shock-tube study [54]. The estimated time-scale of
 6.5 ms is based on OSD and not the true soot inception. The soot inception
height can be crudely approximated as 40 mm from yellow luminosity of the
flame, as discussed in Sec. 2.1. Thus, in a flame-fixed coordinates, the soot
530 inception height is 15 mm , which corresponds to the time-scale of $\sim 4 \text{ ms}$. This
value is quite close to the time delay of 3.5 ms reported by [17]. The present
estimate of 4 ms also includes the fuel evaporation and convection components,
apart from the soot formation chemical time-scale which is $\sim 1 \text{ ms}$.

3.5. Soot and PAH correlations

535 The soot concentration is quantitative, while PAH concentration from LIF is very much qualitative. Nevertheless, certain spatial and intensity correlations between f_v and PAH are noted as discussed in Sec. 3.1. Further statistical trends are explored by considering soot-PAH correlations in different zones of the spray flame. The correlations are evaluated for the H2 field only, where soot
540 inception, peak, and oxidation regions are well captured.

3.5.1. Global soot-PAH correlation

The global maximum of PAH is observed to occur radially well-upstream of the peak- f_v location, as evidenced from instantaneous fields (Sec. 3.1). Thus, instantaneous peak-PAH and peak- f_v locations can differ. To investigate soot-
545 PAH correlation, global maxima (spatial peaks) of soot concentration and PAH are extracted from each of the 2000 realizations. Figure 7a shows the joint PDF between peak- f_v and -PAH. The mode (most probable) peak- f_v measures 1.01 ppm, while mode PAH is 97.2 au. There is a trend of increase in f_v with PAH in Fig. 7a; however, a large spread in f_v is observed for a given PAH inten-
550 sity. The relationship between the imaged smaller-PAH and soot concentration is complex due to various reasons. Smaller-PAH do not directly get converted to soot. Instead, smaller-PAH indirectly contribute to soot formation/growth via larger-PAH. Furthermore, the imaged PAH concentration is the net result of competition of production and consumption processes. Local gas and flow
555 conditions can change the PAH concentration. Additionally, the PAH-LIF signal is only a qualitative indicator of PAH concentration, as explained in Sec. 2.2.2. Besides PAH, the soot formation also depends on local conditions (χ , T , τ), which are not available. These factors explain the large spread in f_v at a given PAH-LIF intensity.

560 To better visualize the f_v and PAH distributions, separate PDFs are plotted in Figs. 7b and 7c. Both f_v and PAH are well-fitted to the log-normal distribution.

3.5.2. Local soot-PAH correlations

Since the soot formation is primarily governed by local conditions, correlations between f_v and PAH-LIF signal are analyzed at three localized regions, namely soot onset, peak, and oxidation as illustrated in Fig. 8.

1. An interrogation window (IW) of 1 *mm* height located 1.5 *mm* downstream of the OSD is considered. The OSD height is defined as a z location where f_v first reaches 0.03 *ppm*, as stated in Sec. 3.4. Recall that soot inception occurs upstream of the OSD. IW regions for different instantaneous images are provided in the Supplementary material, where IW is marked (in blue) on respective instantaneous OH/PAH/soot field for twenty exemplary plots. PAH-LIF intensities are considered only where soot is present (0.03 *ppm* threshold), and therefore the radial domain of IW varies from instant-to-instant.
2. The second region of interest is the peak f_v region. IW of 1 *mm* height around peak f_v location is considered, whereas the radial domain of IW is determined by the soot presence. Examples of peak- f_v IW are provided in the Supplementary material.
3. The third analysis region focuses on local oxidation. The merging of B1-B2 flame branches results in a local flame-tip where soot generally oxidizes (Sec. 3.1). Oxidation IW is centered 1.5 *mm* upstream of the flame-tip (based on the inner OH-layer). IW height is kept 1 *mm*, while the radial domain is restricted to the inner OH-layer. Oxidation IW is overlaid (blue) on respective OH/PAH/soot field, and exemplary plots are provided in the Supplementary material. The B1-B2 merging is observed only in 80% of the total realizations (1600 out of 2000). In the oxidation region, f_v and PAH are expected to be very low, and thus, no lower threshold is applied.

For each IW, two data extraction approaches were used, namely spatial average and spatial maximum within IW. The spatial-average represents semi-local trends, while spatial-maximum provides local statistics at a single pixel. In the spatial-maximum approach, PAH-LIF intensity is extracted at the same

location as of the maximum f_v within IW. In this manner, local conditions are considered.

595 Figures 9a, 9c, and 9e show the joint PDFs of soot-PAH based on spatial average at soot onset, peak, and oxidation regions, respectively. The corresponding PDFs based on spatial maximum are shown on the right panel. Distribution trends are distinct across regions. The spatial average (semi-local) and maximum (local) based approaches yield different distributions. In addition to
600 joint PDFs, individual PDFs of f_v and PAH are provided in Sec. S5 of the Supplement. These PDFs closely conform to the log-normal distribution.

At OSD (Fig. 9a), f_v appears to increase with PAH concentration, although the trend is weaker than the global f_v -PAH correlation (Fig. 7a). The maximum based PDF also shows (Fig. 9b) larger spread in f_v with PAH. As PAH-LIF
605 intensity increases, f_v appear to converge towards the most probable value in both Figs. 9a and 9b. The mean-based PDF in peak f_v region (Fig. 9c) show a more pronounced f_v spread as a function of PAH intensity. The spread in f_v is largest at lower PAH concentrations. A large spread in mean-based correlations is due to the semi-local IW. IW of 1 mm height is considered; however, the radial
610 domain spreads over a larger distance as conditioned on the soot presence (see IW in Supplementary material), as stated earlier. Nevertheless, the f_v range narrows down to the most probable level with an increase in PAH concentration in Fig. 9c. Spatial maximum based PDF (Fig. 9d) is quite different, possibly due to well-defined local conditioning to a single pixel. f_v appears to increase
615 with PAH concentration, albeit with variations. In the oxidation region, very low f_v and PAH signal are observed. The increasing trend of mean f_v with PAH is clear from Fig. 9e. However, the maximum based local approach (Fig. 9f) shows no conclusive trend between f_v and PAH. This is likely due to negligible PAH at a maximum f_v location within oxidation IW.

620 The correlation between the imaged smaller-PAH and soot is not straightforward, as explained in Sec. 3.5.1. Soot formation depends on local conditions, namely scalar dissipation rate, temperature, and residence time (χ , T , τ). The imaged smaller-PAH may have different sensitivity to these local conditions.

Another issue is that the conversion process of smaller-PAH to larger-PAH and
625 eventually to soot in a turbulent flame is a transient phenomenon [12] with
a finite time-scale. Consequently, instantaneous correlations based on random
times (snapshots) may lead to biases since PAH and soot responses to local
time-scale may not be identical. Thus, on instantaneous-basis, PAH do not
strongly correlate with soot concentration. Nevertheless, overall, a weak trend
630 of increase in f_v with PAH is noted in all the considered regions. To investigate
further, time-resolved information of local condition (χ , T , τ), soot, and PAH
(small and large) is needed.

Apart from the distribution trends, f_v and PAH intensities can be compared
across different regions. Most probable values of PAH and f_v from joint PDFs
635 are provided in Table 1, along with the global maxima. The trends in the spa-
tial mean- and maximum-based quantities are identical. The maximum-based
local PAH values are lower than mean-based values since PAH in a maximum
approach is considered only at a maximum f_v position. From soot onset to
peak region, f_v and PAH are inversely correlated as expected since smaller-
640 PAH eventually assist in the soot formation/growth via larger-PAH. From soot
peak to oxidation region, both f_v and PAH decrease, as soot gets oxidized in the
flame-tip region. As expected, both PAH and soot concentrations approach zero
upstream of the local flame-tip (oxidation) region. Both PAH and f_v intensities
vary over a large range, as evidenced from the difference between global maxima
645 and oxidation region values.

3.5.3. Spatial soot-PAH correlations

The previous section explored intensity-based soot-PAH joint statistics in
which the PAH intensity is very much qualitative. Alternatively, a spatial cor-
relation between soot and PAH can be obtained. For spatial correlations, only
650 the signal presence is relevant rather than the absolute intensity. Consequently,
the derived conclusions can be more robust.

In Sec. 3.1, spatial overlap between the soot and PAH structures is discussed
with a few instantaneous fields. To exploit all the available realizations (2000),

the spatial correlation statistics are evaluated. Three regions namely soot onset,
655 peak, and oxidation regions (illustrated in Fig. 8) are further analyzed. The
interrogation windows are identical as described in Sec. 3.5.2. To define the
soot presence, a threshold of 0.03 ppm was used, while the PAH presence is
set to 350 counts (3.5 au) of LIF intensity, similar to Sec. 3.3. The extent of
PAH overlap relative to the soot is deduced from binarized images. The spatial
660 correlation index varies from 0 (no overlap) to 1 (100% overlap). Each instant
provides an IW-averaged spatial correlation index. The index is evaluated for
all the realizations, and PDFs are presented in Fig. 10. The mean (μ), stan-
dard deviations (σ), and mode (most probable, m) values are indicated on the
respective PDF.

665 Additionally, an intensity correlation is deduced by taking a pixel-by-pixel
product of PAH-LIF signal with f_v . Since the intensity is of interest, no lower
threshold is applied to either f_v or PAH signal. Instead, f_v and PAH intensities
are conditioned within respective IW. The soot-PAH product intensities are
averaged over IW area. PDFs of such 2000 spatially-averaged soot-PAH product
670 values are shown in Fig. 11. PDFs exhibit the log-normal distribution, similar
to individual distributions of f_v and PAH (provided in Fig. S4).

In the soot onset region, PAH and soot overlap is 100% most of the time,
with a time-averaged mean overlap of 87% as noted from Fig. 10a. Despite the
overlap, product of f_v and PAH signal (Fig. 11a) is moderate due to low f_v in the
675 OSD region. At peak soot regions, PAH and soot overlap (Fig. 10b) is significant
($m = 84\%$) with time-averaged mean overlap of 71%. The soot-PAH product
intensity is highest (Fig. 11b) due to higher f_v accompanied by a moderate
PAH concentration. In the oxidation region, PAH and soot overlap (Fig. 10c)
is relatively low ($m = 36\%$). Occasionally, no overlap is observed, suggesting
680 complete consumption of PAH near oxidation region. The largest fluctuation
in soot-PAH overlap occurs in the oxidation region ($\sigma = 0.26$), indicating the
intermittent nature of soot oxidation. The corresponding soot-PAH product
(Fig. 11c) is the lowest due to lower soot and PAH concentrations; however, the
fluctuation intensity (σ/μ) is the highest. In summary, the soot-PAH overlap

685 decreases consistently from the soot onset to oxidation region due to the smaller-
PAH conversion to larger-PAH that subsequently lead to soot. The largest
fluctuations exist in the soot oxidation region.

4. Conclusions

Soot formation in the turbulent *n*-heptane spray flame is studied through
690 quantitative soot volume fraction (f_v) using LII. Additionally, the soot-precursor
(PAH) and flame front (OH) are imaged simultaneously using PLIF. f_v /OH/PAH
fields are analyzed based on instantaneous and mean structures. Furthermore,
joint statistics between f_v and PAH are deduced to explore the spatial and
intensity correlations in various regions.

695 The spray flame consisted of an annular dual branch structure. The inner
branch B1 is composed of adjacent fuel-lean and non-premixed reaction zones,
whereas the outer branch B2 is purely non-premixed [30]. B1/B2 frequently
(80%) merges, forming a local flame-tip. Local extinctions are observed in B1
due to traversing fuel droplets and high strain rate, while no extinctions are
700 noted in B2 due to lower strain rate. Soot inception always occurs near B2
(towards the fuel-rich side) due to soot-favorable conditions, namely lower scalar
dissipation rate and longer residence time. The radial order of species in the
inception region is as follows: B1, PAH, soot, and B2, where soot sheet occupies
only a small area of the PAH cloud. At downstream regions, soot structures
705 begin to spread over the entire PAH zone, suggesting a rapid soot growth. Soot
is also observed near B1, but well-downstream of local extinction regions. Soot
and PAH concentrations upstream of the local flame-tip are negligible, as soot
gets oxidized rapidly across the flame-front. In general, soot and OH layers do
not overlap due to soot oxidation by OH. The influence of local flame extinctions
710 and lift-off height fluctuations on soot behavior is also investigated. Both of
these parameters do not instantaneously influence the global f_v , likely due to a
time delay in soot response.

There exists high temporal soot intermittency. Instantaneous peak f_v typi-

cally varies in $0.2 - 5$ ppm range with the most probable value of 1 ppm. The
715 soot presence probability is only 0.6 at the most due to the intermittent nature
of soot formation. To avoid intermittency biases, a conditional average is de-
duced. The conditionally averaged spatial peak f_v measures 0.42 ppm, which is
2.5 times as of the unconditional mean. The conditional mean does not show
any decrease in f_v with the height that was observed in unconditional mean
720 owing to the soot intermittency.

Interpretation of soot-PAH correlation is challenging since soot formation
also depends on the scalar dissipation rate, temperature, and residence time.
Additionally, there may be a time delay in a soot response to a change in con-
ditions, even locally. Nevertheless, few distinct trends are noted. The f_v and
725 PAH intensities generally conform to the log-normal distributions. Distinct joint
PDFs of soot-PAH are observed in soot onset, peak, and oxidation regions. A
weaker trend of increase in f_v with PAH intensity is noted, without any strong
correlations. The most probable PAH intensity show a decreasing trend from
onset to peak soot region. Additionally, the soot-PAH overlap decreases from
730 onset to oxidation (flame-tip) region. These observations suggest the possible
conversion of smaller-PAH to eventually form soot (via larger-PAH) with in-
creasing height (residence time), consistent with gas-fueled flames. The largest
intensity and spatial-overlap fluctuations exist in the oxidation region, likely
due to temperature variations near the flame-tip region.

735 Through simultaneous imaging and detailed analysis, the present work con-
tributes to sooting turbulent spray combustion field on three fronts namely, soot
database for model validations, identification of soot onset and oxidation zones,
and analysis of soot-PAH correlations at different stages of soot maturity. Fur-
ther insights into the soot-PAH and soot-flame correlations require time-resolved
740 data with additional quantities, namely larger-PAH, temperature, mixing field,
and velocity field.

Acknowledgments

The authors are grateful for the financial support of Safran Aircraft Engines and the French National Research Agency (Industrial chair PERCEVAL ANR-745 15-CHIN-0001). Dr. I.A. Mulla is the recipient of a Marie Skłodowska-Curie Individual Fellowship (ID: 747576) awarded by the European Commission under H2020-EU.1.3.2 scheme. The assistance of Dr. G. Godard in laser installation and Mr. A. Vandel in burner installation is gratefully acknowledged.

Table 1: Most probable f_v (in *ppm*) and PAH-LIF intensity (in *au*) at various soot regions.

| Soot region | Mean based | | Max. based | |
|--------------------|------------|------|------------|------|
| | f_v | PAH | f_v | PAH |
| <i>Global max.</i> | - | - | 1.01 | 97.4 |
| <i>OSD</i> | 0.05 | 9.1 | 0.09 | 5.7 |
| <i>Peak</i> | 0.30 | 4.3 | 0.96 | 3.7 |
| <i>Oxidation</i> | 0.00 | 0.05 | 0.00 | 0.0 |

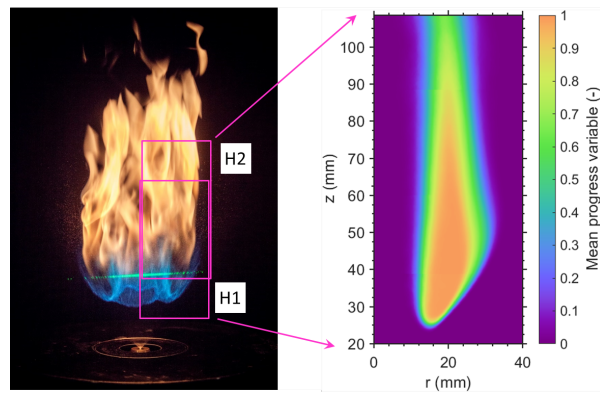


Figure 1: Flame photograph and mean progress variable (from OH-PLIF).

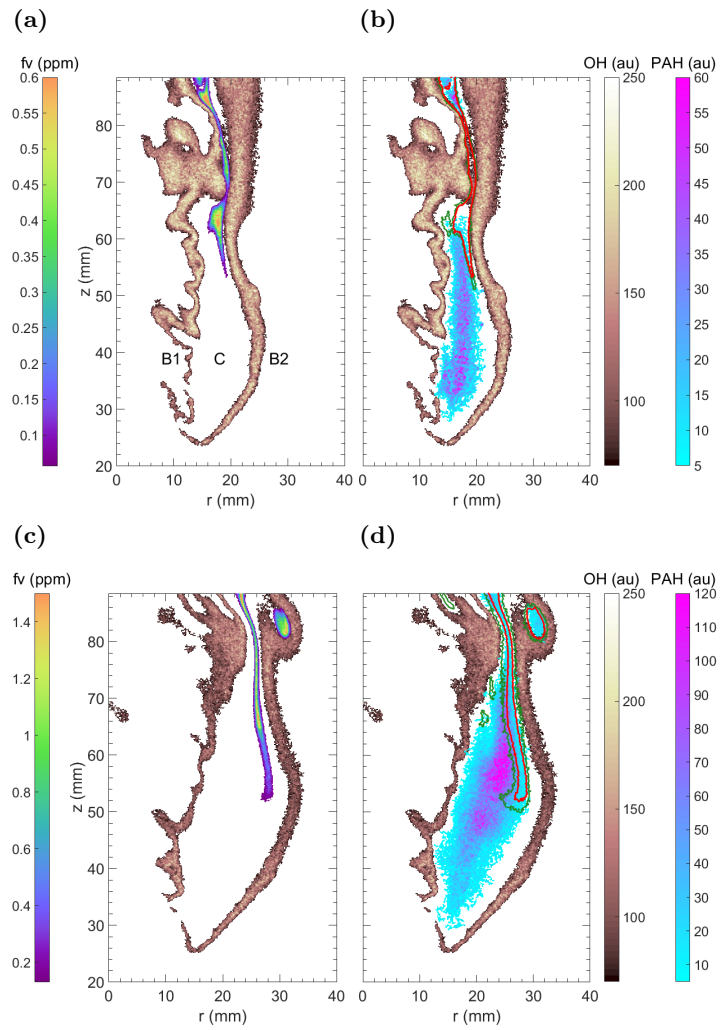


Figure 2: Instantaneous fields at H1: (a, c) OH-PLIF and f_v , (b, d) OH/PAH PLIF with f_v isocontours (red: 7% of peak, green: 0.03 ppm).

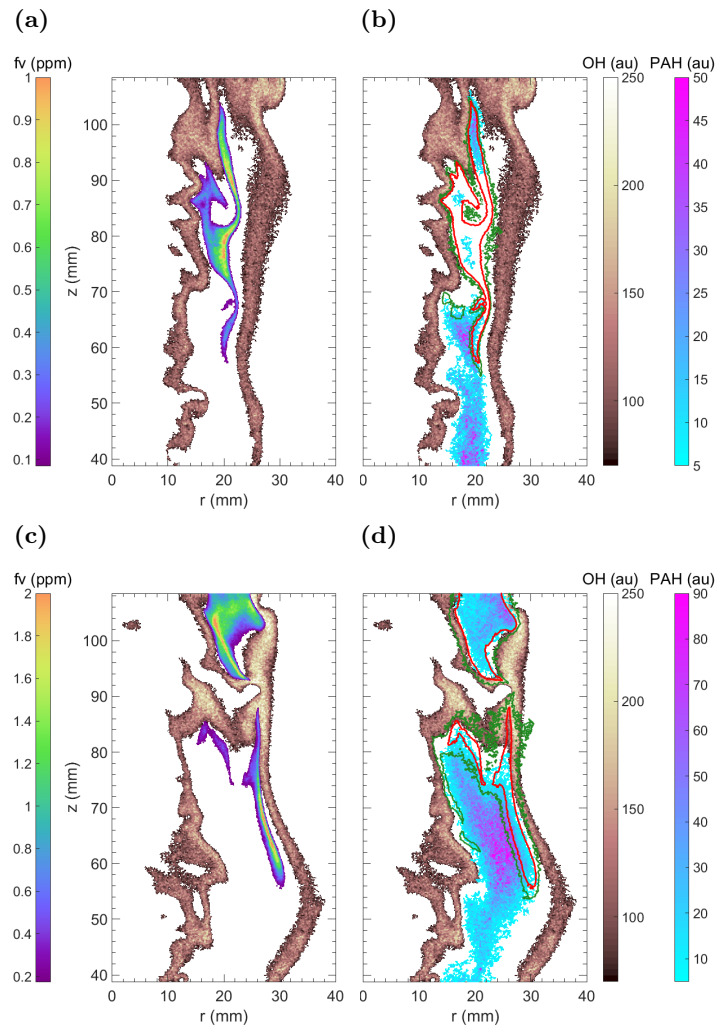


Figure 3: Instantaneous fields at H2: (a, c) OH-PLIF and f_v , (b, d) OH/PAH PLIF with f_v isocontours (red: 7% of peak, green: 0.03 ppm).

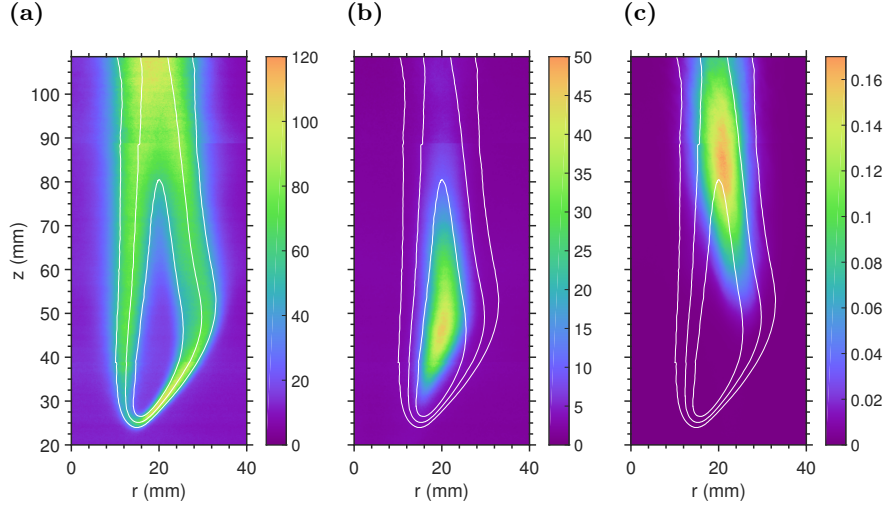


Figure 4: Time-averaged fields: (a) OH-PLIF in au , (b) PAH-PLIF in au , (c) soot volume fraction f_v^U in ppm , with \bar{c} contours of 0.1 (outer), 0.5, and 0.9 (inner). The superscript U signifies unconditional average.

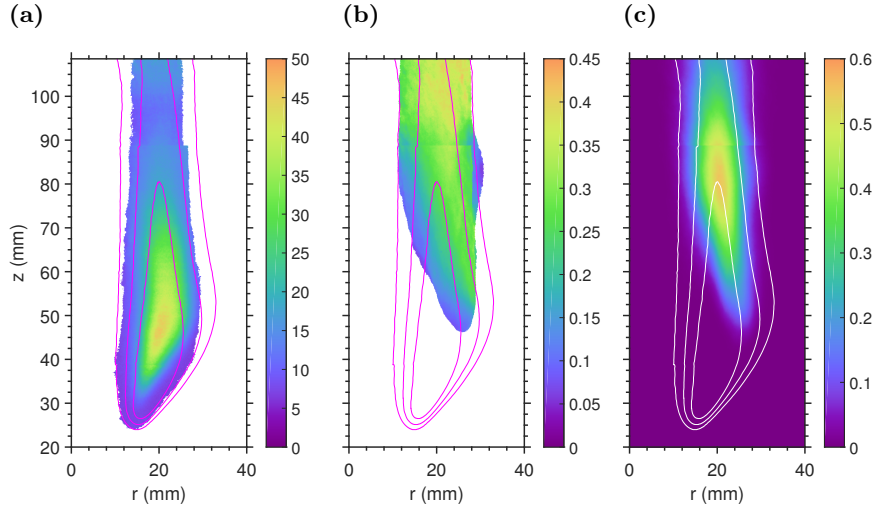


Figure 5: Conditional mean fields: (a) PAH-PLIF in au , (b) f_v^C in ppm . (c) soot presence probability, with \bar{c} contours of 0.1 (outer), 0.5, and 0.9 (inner).

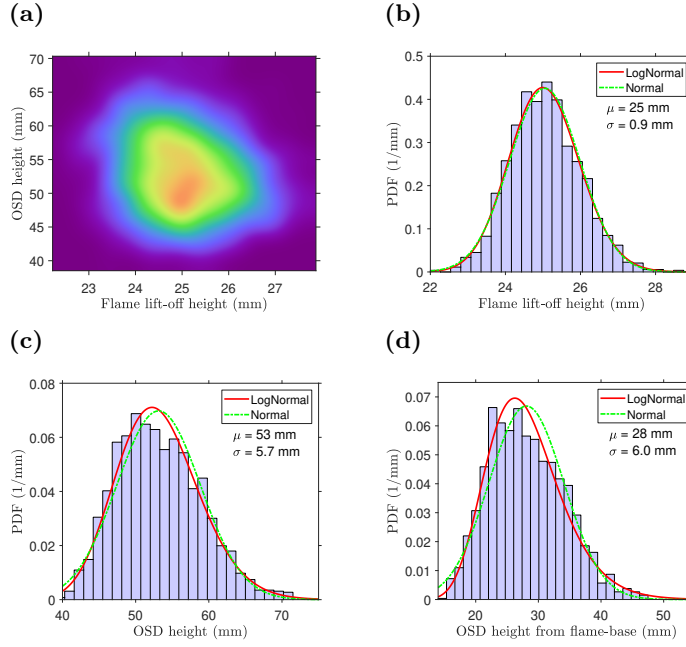


Figure 6: Flame-lift off height and OSD height correlation: (a) joint PDF (blue and red corresponds to minimum and maximum, respectively), (b) PDF of h_{lift} , (c) PDF of h_{OSD} , (d) PDF of $h_{OSD} - h_{lift}$.

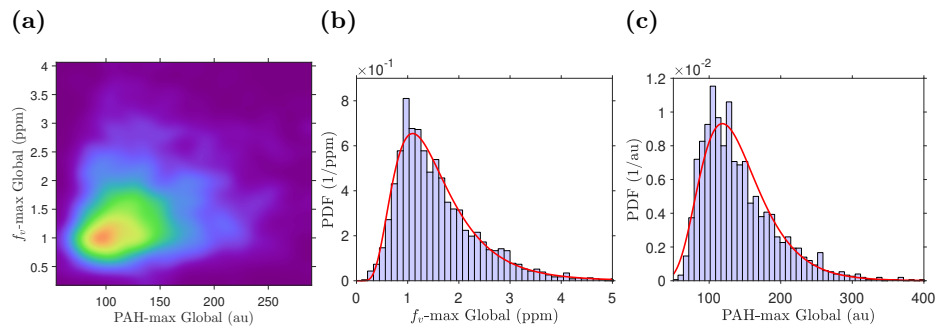


Figure 7: Global maximum: (a) joint PDF of f_v and PAH (blue and red corresponds to minimum and maximum, respectively), (b) f_v PDF with log-normal fit, (c) PAH PDF with log-normal fit.

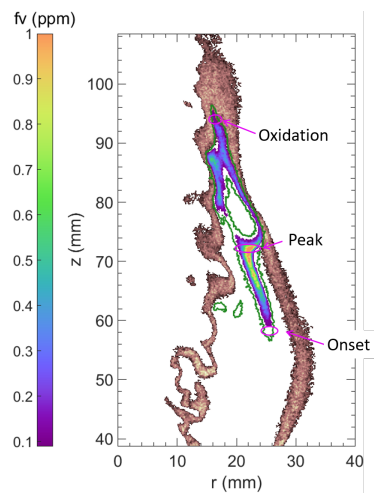


Figure 8: Soot onset, peak, and oxidation interrogation windows illustrated on soot/OH instant. The isocontour of 0.03 ppm is marked in green.

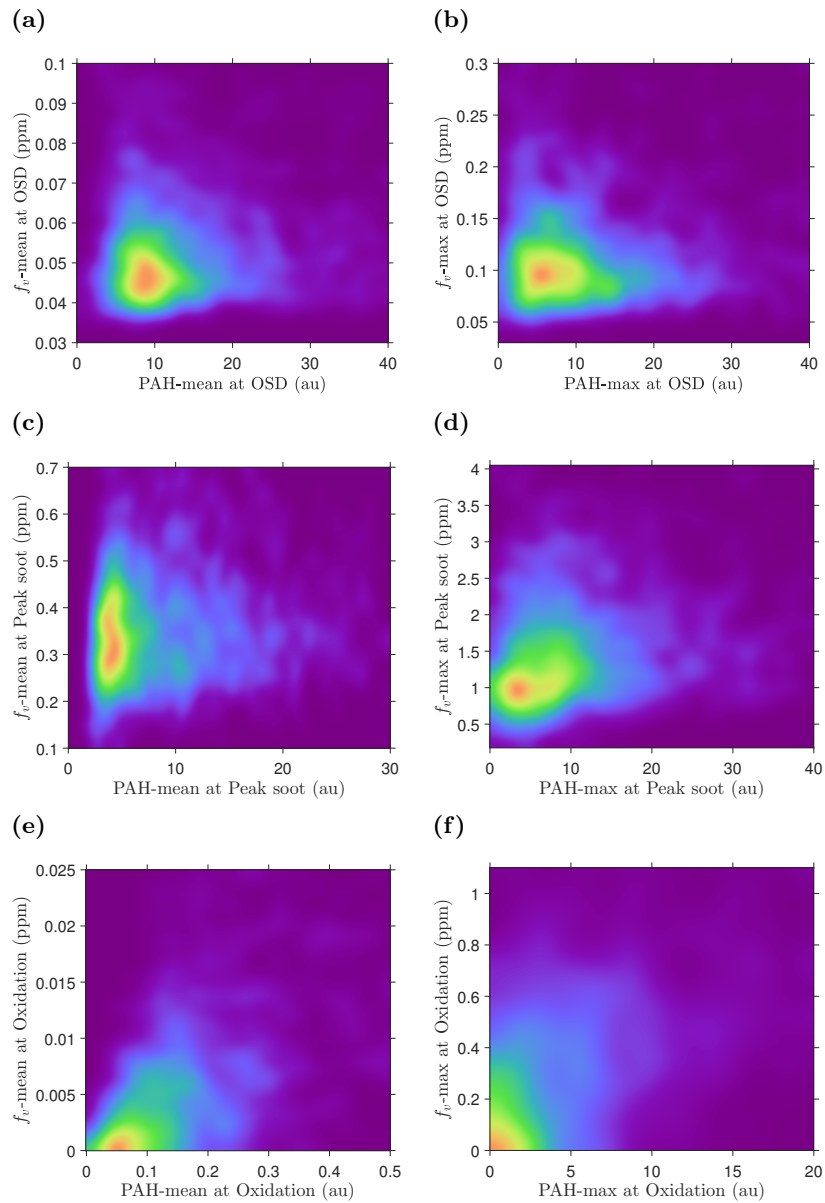


Figure 9: Joint PDFs of f_v and PAH: (a) mean (b) maximum at soot onset, (c) mean (d) maximum at soot peak, and (e) mean (f) maximum at soot oxidation. Blue and red corresponds to minimum and maximum probabilities, respectively.

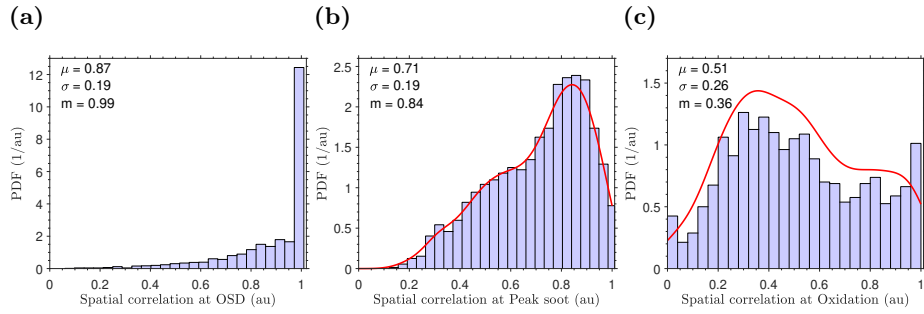


Figure 10: Spatial correlation index between f_v and PAH at soot: (a) onset, (b) peak, (c) oxidation regions. Red curves show a non-parametric kernel density estimate. Mean (μ), standard deviation (σ), and mode (m) are listed on respective PDF.

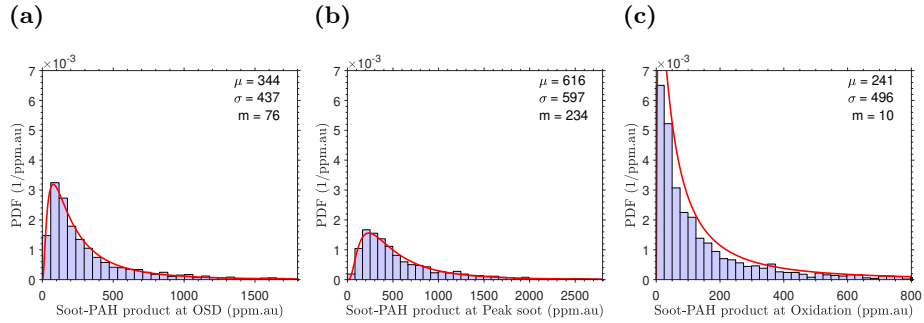


Figure 11: Product of f_v and PAH-LIF intensity at soot: (a) onset, (b) peak, (c) oxidation regions. Legends are identical as of Fig. 10

References

- 750 [1] D. Shindell, J. C. I. Kuylensstierna, E. Vignati, R. van Dingenen, M. Amann, Z. Klimont, S. C. Anenberg, N. Muller, G. Janssens-Maenhout, F. Raes, J. Schwartz, G. Faluvegi, L. Pozzoli, K. Kupiainen, L. Hoglund-Isaksson, L. Emberson, D. Streets, V. Ramanathan, K. Hicks, N. T. K. Oanh, G. Milly, M. Williams, V. Demkine, D. Fowler, Simultaneously mitigating
755 near-term climate change and improving human health and food security, *Science* 335 (6065) (2012) 183–189. doi:[10.1126/science.1210026](https://doi.org/10.1126/science.1210026).
- [2] C. R. Shaddix, J. Zhang, R. W. Schefer, J. Doom, J. C. Oefelein, S. Kook, L. M. Pickett, H. Wang, Understanding and predicting soot generation in turbulent non-premixed jet flames, Tech. Rep. Sand2010-7178, Sandia
760 National Laboratories (1999).
- [3] D. Gu, Z. Sun, B. B. Dally, P. R. Medwell, Z. T. Alwahabi, G. J. Nathan, Simultaneous measurements of gas temperature, soot volume fraction and primary particle diameter in a sooting lifted turbulent ethylene/air non-premixed flame, *Combust. Flame* 179 (2017) 33–50. doi:
765 [10.1016/j.combustflame.2017.01.017](https://doi.org/10.1016/j.combustflame.2017.01.017).
- [4] M. Köhler, K. P. Geigle, W. Meier, B. M. Crosland, K. A. Thomson, G. J. Smallwood, Sooting turbulent jet flame: characterization and quantitative soot measurements, *Appl. Phys. B* 104 (2) (2011) 409–425. doi:
[10.1007/s00340-011-4373-y](https://doi.org/10.1007/s00340-011-4373-y).
- 770 [5] M. Köhler, K.-P. Geigle, T. Blacha, P. Gerlinger, W. Meier, Experimental characterization and numerical simulation of a sooting lifted turbulent jet diffusion flame, *Combust. Flame* 159 (8) (2012) 2620–2635. doi:[10.1016/j.combustflame.2012.01.015](https://doi.org/10.1016/j.combustflame.2012.01.015).
- 775 [6] P. Rodrigues, B. Franzelli, R. Vicquelin, O. Gicquel, N. Darabiha, Coupling an LES approach and a soot sectional model for the study of sooting turbulent non-premixed flames, *Combust. Flame* 190 (2018) 477–499. doi:[10.1016/j.combustflame.2017.12.009](https://doi.org/10.1016/j.combustflame.2017.12.009).

- [7] O. Park, R. A. Burns, N. T. Clemens, Relationship between soot and scalar dissipation rate in the soot-inception region of turbulent non-premixed jet flames, Proc. Combust. Inst. 37 (1) (2019) 1057–1064. doi:10.1016/j.proci.2018.06.174.
- [8] S. Kruse, J. Ye, Z. Sun, A. Attili, B. Dally, P. Medwell, H. Pitsch, Experimental investigation of soot evolution in a turbulent non-premixed prevaporized toluene flame, Proc. Combust. Inst. 37 (1) (2019) 849–857. doi:10.1016/j.proci.2018.05.075.
- [9] F. Bisetti, G. Blanquart, M. E. Mueller, H. Pitsch, On the formation and early evolution of soot in turbulent nonpremixed flames, Combust. Flame 159 (1) (2012) 317–335. doi:10.1016/j.combustflame.2011.05.021.
- [10] V. Narayanaswamy, N. Clemens, Simultaneous LII and PIV measurements in the soot formation region of turbulent non-premixed jet flames, Proc. Combust. Inst. 34 (1) (2013) 1455–1463. doi:10.1016/j.proci.2012.06.018.
- [11] S. Mahmoud, T. Lau, G. Nathan, P. Medwell, Z. Alwahabi, B. Dally, A new correlation between soot sheet width and soot volume fraction in turbulent non-premixed jet flames, Proc. Combust. Inst. 37 (1) (2019) 927–934. doi:10.1016/j.proci.2018.06.108.
- [12] B. Franzelli, P. Scouffaire, S. Candel, Time-resolved spatial patterns and interactions of soot, PAH and OH in a turbulent diffusion flame, Proc. Combust. Inst. 35 (2) (2015) 1921–1929. doi:10.1016/j.proci.2014.06.123.
- [13] B. M. Crosland, K. A. Thomson, M. R. Johnson, Simultaneous instantaneous measurements of soot volume fraction, primary particle diameter, and aggregate size in turbulent buoyant diffusion flames, Proc. Combust. Inst. 35 (2) (2015) 1851–1859. doi:10.1016/j.proci.2014.06.003.

- 805 [14] K. P. Geigle, W. O’Loughlin, R. Hadeif, W. Meier, Visualization of soot inception in turbulent pressurized flames by simultaneous measurement of laser-induced fluorescence of polycyclic aromatic hydrocarbons and laser-induced incandescence, and correlation to OH distributions, *Appl. Phys. B* 119 (4) (2015) 717–730. [doi:10.1007/s00340-015-6075-3](https://doi.org/10.1007/s00340-015-6075-3).
- 810 [15] K. P. Geigle, M. Köhler, W. O’Loughlin, W. Meier, Investigation of soot formation in pressurized swirl flames by laser measurements of temperature, flame structures and soot concentrations, *Proc. Combust. Inst.* 35 (3) (2015) 3373–3380. [doi:10.1016/j.proci.2014.05.135](https://doi.org/10.1016/j.proci.2014.05.135).
- [16] K. P. Geigle, R. Hadeif, M. Stöhr, W. Meier, Flow field characterization of pressurized sooting swirl flames and relation to soot distributions, *Proc. Combust. Inst.* 36 (3) (2017) 3917–3924. [doi:10.1016/j.proci.2016.09.024](https://doi.org/10.1016/j.proci.2016.09.024).
- 820 [17] M. Stöhr, K. Geigle, R. Hadeif, I. Boxx, C. Carter, M. Grader, P. Gerlinger, Time-resolved study of transient soot formation in an aero-engine model combustor at elevated pressure, *Proc. Combust. Inst.* 37 (4) (2019) 5421–5428. [doi:10.1016/j.proci.2018.05.122](https://doi.org/10.1016/j.proci.2018.05.122).
- [18] M. Roussillo, P. Scoufflaire, S. Candel, B. Franzelli, Experimental investigation of soot production in a confined swirled flame operating under perfectly premixed rich conditions, *Proc. Combust. Inst.* 37 (1) (2019) 893–901. [doi:10.1016/j.proci.2018.06.110](https://doi.org/10.1016/j.proci.2018.06.110).
- 825 [19] A. Wick, F. Priesack, H. Pitsch, Large-eddy simulation and detailed modeling of soot evolution in a model aero engine combustor, in: Volume 4A: Combustion, Fuels and Emissions, ASME, 2017. [doi:10.1115/gt2017-63293](https://doi.org/10.1115/gt2017-63293).
- 830 [20] B. Franzelli, A. Vié, N. Darabiha, A three-equation model for the prediction of soot emissions in LES of gas turbines, *Proc. Combust. Inst.* 37 (4) (2019) 5411–5419. [doi:10.1016/j.proci.2018.05.061](https://doi.org/10.1016/j.proci.2018.05.061).

- [21] International sooting flame (ISF) workshop, <https://www.adelaide.edu.au/cet/isfworkshop/data-sets/turbulent/> (Accessed on 2019-07-17).
- 835 [22] K. Inagaki, S. Takasu, K. Nakakita, In-cylinder quantitative soot concentration measurement by laser-induced incandescence, in: SAE Technical Paper Series, SAE International, 1999. doi:10.4271/1999-01-0508.
- [23] S. A. Skeen, J. Manin, L. M. Pickett, E. Cenker, G. Bruneaux, K. Kondo, T. Aizawa, F. Westlye, K. Dalen, A. Ivarsson, T. Xuan, J. M. Garcia-Oliver, Y. Pei, S. Som, W. Hu, R. D. Reitz, T. Lucchini, G. D'Errico, 840 D. Farrace, S. S. Pandurangi, Y. M. Wright, M. A. Chishty, M. Bolla, E. Hawkes, A progress review on soot experiments and modeling in the engine combustion network (ECN), SAE Int. J. Engines 9 (2) (2016) 883–898. doi:10.4271/2016-01-0734.
- 845 [24] L. Pickett, G. Bruneaux, R. Payri, Engine combustion network, <https://ecn.sandia.gov/> (Accessed on 2019-07-17).
- [25] 6th workshop on measurement and computation of turbulent spray combustion, September 17, 2017, Naples, Italy, <http://www.tcs-workshop.org/tcs6.html> (Accessed on 2019-07-17).
- 850 [26] T. R. Meyer, S. Roy, V. M. Belovich, E. Corporan, J. R. Gord, Simultaneous planar laser-induced incandescence, OH planar laser-induced fluorescence, and droplet mie scattering in swirl-stabilized spray flames, Appl. Opt. 44 (3) (2005) 445. doi:10.1364/ao.44.000445.
- [27] L.-Y. Wang, C. K. Bauer, O. L. Gülder, Soot and flow field in turbulent 855 swirl-stabilized spray flames of jet A-1 in a model combustor, Proc. Combust. Inst. 37 (4) (2019) 5437–5444. doi:10.1016/j.proci.2018.05.093.
- [28] A. Verdier, J. M. Santiago, A. Vandel, S. Saengkaew, G. Cabot, G. Grehan, B. Renou, Experimental study of local flame structures and fuel droplet properties of a spray jet flame, Proc. Combust. Inst. 36 (2017) 2595–2602. 860 doi:10.1016/j.proci.2016.07.016.

- [29] A. Verdier, J. M. Santiago, A. Vandiel, G. Godard, G. Cabot, B. Renou, Local extinction mechanisms analysis of spray jet flame using high speed diagnostics, *Combust. Flame* 193 (2018) 440–452. doi:10.1016/j.combustflame.2018.03.032.
- 865 [30] F. Shum-Kivan, J. M. Santiago, A. Verdier, E. Riber, B. Renou, G. Cabot, B. Cuenot, Experimental and numerical analysis of a turbulent spray flame structure, *Proc. Combust. Inst.* 36 (2017) 2567–2575. doi:10.1016/j.proci.2016.06.039.
- 870 [31] I. A. Mulla, G. Godard, G. Cabot, F. Grisch, B. Renou, Quantitative imaging of nitric oxide concentration in a turbulent n-heptane spray flame, *Combust. Flame* 203 (2019) 217–229. doi:10.1016/j.combustflame.2019.02.005.
- 875 [32] I. A. Mulla, G. Godard, B. Renou, Instantaneous planar measurements of nitric oxide concentration in a turbulent n-heptane spray flame, *Combust. Flame* 208 (2019) 451–471. doi:10.1016/j.combustflame.2019.07.026.
- [33] J. D. Gounder, A. Kourmatzis, A. R. Masri, Turbulent piloted dilute spray flames: Flow fields and droplet dynamics, *Combust. Flame* 159 (11) (2012) 3372–3397. doi:10.1016/j.combustflame.2012.07.014.
- 880 [34] R. Yuan, J. Kariuki, A. Dowlut, R. Balachandran, E. Mastorakos, Reaction zone visualisation in swirling spray n -heptane flames, *Proc. Combust. Inst.* 35 (2) (2015) 1649–1656. doi:10.1016/j.proci.2014.06.012.
- [35] R. Yuan, J. Kariuki, E. Mastorakos, Measurements in swirling spray flames at blow-off, *Int. J. Spray Combust. Dyn.* 10 (3) (2018) 185–210. doi:10.1177/1756827718763559.
- 885 [36] C. Schulz, B. Kock, M. Hofmann, H. Michelsen, S. Will, B. Bougie, R. Suntz, G. Smallwood, Laser-induced incandescence: recent trends and current questions, *Appl. Phys. B* 83 (3) (2006) 333–354. doi:10.1007/s00340-006-2260-8.

- [37] S. Bejaoui, X. Mercier, P. Desgroux, E. Therssen, Laser induced fluorescence spectroscopy of aromatic species produced in atmospheric sooting flames using UV and visible excitation wavelengths, *Combust. Flame* 161 (10) (2014) 2479–2491. doi:10.1016/j.combustflame.2014.03.014. 890
- [38] R. Hadeif, K. P. Geigle, W. Meier, M. Aigner, Soot characterization with laser-induced incandescence applied to a laminar premixed ethylene–air flame, *Int. J. of Therm. Sci.* 49 (8) (2010) 1457–1467. doi:10.1016/j.ijthermalsci.2010.02.014. 895
- [39] A. Cessou, D. Stepowski, Planar laser induced fluorescence measurement of [OH] in the stabilization stage of a spray jet flame, *Combust. Sci. Technol.* 118 (4-6) (1996) 361–381. doi:10.1080/00102209608951986.
- [40] J. Luque, D. Crosley, LIFBASE: Database and spectral simulation program (version 2.1.1), Tech. Rep. MP 99-009, SRI International (1999). 900
- [41] N.-E. Olofsson, H. Bladh, A. Bohlin, J. Johnsson, P.-E. Bengtsson, Are sooting premixed porous-plug burner flames one-dimensional? A laser-based experimental investigation, *Combust. Sci. Technol.* 185 (2) (2013) 293–309. doi:10.1080/00102202.2012.718006. 905
- [42] T. Mouton, X. Mercier, P. Desgroux, Isomer discrimination of PAHs formed in sooting flames by jet-cooled laser-induced fluorescence: application to the measurement of pyrene and fluoranthene, *Appl. Phys. B* 122 (5) (2016) 123. doi:10.1007/s00340-016-6397-9.
- [43] P. Desgroux, X. Mercier, K. A. Thomson, Study of the formation of soot and its precursors in flames using optical diagnostics, *Proc. Combust. Inst.* 34 (1) (2013) 1713–1738. doi:10.1016/j.proci.2012.09.004. 910
- [44] H. Nakamura, R. Tanimoto, T. Tezuka, S. Hasegawa, K. Maruta, Soot formation characteristics and PAH formation process in a micro flow reactor with a controlled temperature profile, *Combust. Flame* 161 (2) (2014) 582–591. doi:10.1016/j.combustflame.2013.09.004. 915

- [45] A. D’Anna, M. Commodo, M. Sirignano, P. Minutolo, R. Pagliara, Particle formation in opposed-flow diffusion flames of ethylene: An experimental and numerical study, *Proc. Combust. Inst.* 32 (1) (2009) 793–801. doi:
920 [10.1016/j.proci.2008.06.200](https://doi.org/10.1016/j.proci.2008.06.200).
- [46] F. Shum-Kivan, Simulation des grandes echelles de flammes de spray et modélisation de la combustion non-prémélangée, Ph.D. thesis, Université de Toulouse, France (2017).
- [47] H. Guo, P. M. Anderson, P. B. Sunderland, Optimized rate expressions for
925 soot oxidation by OH and O₂, *Fuel* 172 (2016) 248–252. doi:[10.1016/j.fuel.2016.01.030](https://doi.org/10.1016/j.fuel.2016.01.030).
- [48] R. Puri, R. J. Santoro, K. C. Smyth, The oxidation of soot and carbon monoxide in hydrocarbon diffusion flames, *Combust. Flame* 97 (2) (1994) 125–144. doi:[10.1016/0010-2180\(94\)90001-9](https://doi.org/10.1016/0010-2180(94)90001-9).
- 930 [49] P. Singh, C.-J. Sung, PAH formation in counterflow non-premixed flames of butane and butanol isomers, *Combust. Flame* 170 (2016) 91–110. doi:
[10.1016/j.combustflame.2016.05.009](https://doi.org/10.1016/j.combustflame.2016.05.009).
- [50] C. Law, Dynamics of stretched flames, *Symp. (Int.) Combust.* 22 (1) (1989) 1381–1402. doi:[10.1016/s0082-0784\(89\)80149-3](https://doi.org/10.1016/s0082-0784(89)80149-3).
- 935 [51] N. Qamar, Z. Alwahabi, Q. Chan, G. Nathan, D. Roekaerts, K. King, Soot volume fraction in a piloted turbulent jet non-premixed flame of natural gas, *Combust. Flame* 156 (7) (2009) 1339–1347. doi:
[10.1016/j.combustflame.2009.02.011](https://doi.org/10.1016/j.combustflame.2009.02.011).
- 940 [52] M. Leschowski, K. A. Thomson, D. R. Snelling, C. Schulz, G. J. Smallwood, Combination of LII and extinction measurements for determination of soot volume fraction and estimation of soot maturity in non-premixed laminar flames, *Appl. Phys. B* 119 (4) (2015) 685–696. doi:
[10.1007/s00340-015-6092-2](https://doi.org/10.1007/s00340-015-6092-2).

- 945 [53] Z. I. Botev, J. F. Grotowski, D. P. Kroese, Kernel density estimation via diffusion, *Ann. Stat.* 38 (5) (2010) 2916–2957. doi:[10.1214/10-aos799](https://doi.org/10.1214/10-aos799).
- [54] Z. Hong, D. Davidson, S. Vasu, R. Hanson, The effect of oxygenates on soot formation in rich heptane mixtures: A shock tube study, *Fuel* 88 (10) (2009) 1901–1906. doi:[10.1016/j.fuel.2009.04.013](https://doi.org/10.1016/j.fuel.2009.04.013).